Journal of Science: Advanced Materials and Devices 7 (2022) 100466

Contents lists available at ScienceDirect

Journal of Science: Advanced Materials and Devices

journal homepage: www.elsevier.com/locate/jsamd

Original Article

Effect of the modified hybrid particle on the corrosion inhibition performance of polyolefin based coatings for carbon steel

Sehrish Habib [a, c], Muddasir Nawaz [a], Ramazan Kahraman [b, **], Elsadig Mahdi Ahmed [c], R.A. Shakoor [a, *]

[a] Center for Advanced Materials (CAM), Qatar University, 2713, Doha, Qatar
[b] Department of Chemical Engineering, Qatar University, 2713, Doha, Qatar
[c] Department of Mechanical and Industrial Engineering, Qatar University, 2713, Doha, Qatar

ARTICLE INFO

Article history:
Received 6 March 2022
Received in revised form
14 April 2022
Accepted 23 April 2022
Available online 14 May 2022

Keywords:
Polyolefin
Cerium oxide
Zinc oxide
Benzotriazole
EIS
Corrosion inhibition

ABSTRACT

This work reports the corrosion inhibition performance of modified hybrid particles reinforced into polyolefin matrix. The cerium oxide coated zinc oxide hybrid particles (CeO_2@ZnO) were synthesized via a chemical precipitation process. The synthesized hybrid particles were modified with benzotriazole (BTA, corrosion inhibitor). The modified hybrid particles were reinforced into a polyolefin matrix in 1 wt. % concentration. Transmission electron microscopy (TEM), Fourier transform infrared spectroscopy (FTIR), Thermogravimetric analysis (TGA), energy dispersive X-Ray spectroscopy (EDX), and X-ray photoelectron spectrometer (XPS) analysis techniques were employed to characterize synthesized and modified hybrid particles. The results demonstrated that ZnO possessed hexagonal morphology covered with spherical CeO_2 particles. FTIR analysis revealed the presence of characteristic peaks of the modified hybrid particles. TGA analysis demonstrated good thermal stability of synthesized particles. UV-vis spectroscopic analysis confirmed the release of the inhibitor from hybrid particle, which was pH and time-dependent. The modified polymeric coatings' self-healing functioning was evaluated through Electrochemical impedance spectroscopic analysis. The results revealed the prominent corrosion inhibition performance of the modified coatings compared to the blank polyolefin coatings, which is attributed to the efficient release of the inhibitor from hybrid particles, making these coatings a promising solution for the protection of steel.

1. Introduction

Corrosion of metallic assets is the most crucial cause of components and equipment failure, resulting in serious economic losses. In the Oil & Gas sector, it has been demonstrated that corrosion problems are the main responsible of equipment and component failure. The consequence is that operation and maintenance (O&M) costs can easily reach 50% of the total cost of the infrastructure; out of these costs, around 80% are due to corrosion damage [1,2]. Thus, corrosion is a serious problem for industry competitiveness, being responsible for the very high operational expenditures (OPEX) in many industrial sectors and has a very negative impact on the economic performance of the infrastructures and the infrastructure's lifetime.

A very effective route to protect metallic (and non-metallic) assets against corrosion is applying protective organic coatings. Organic coatings can comprise polymeric matrix, carriers, corrosion inhibitors, and other functional species [3]. Protective coatings must ensure high barrier properties and mechanical strength, the reason why they are typically multilayered and thick, dense, and non-porous. Polyolefin coatings have excellent mechanical properties and display very efficient polymer healing ability. Moreover, polyolefin coatings are easy to apply and economically competitive [4]. However, there is still a critical barrier to progress with polyolefin coating because they weakly inhibit corrosion propagation at the metal interface. This is due to highly susceptible matrices. To overcome these drawbacks, a highly promising strategy explores the smart delivery of corrosion inhibiting species stored in

* Corresponding author.
** Corresponding author.
E-mail addresses: ramazank@qu.edu.qa (R. Kahraman), shakoor@qu.edu.qa (R.A. Shakoor).

Peer review under responsibility of Vietnam National University, Hanoi.

https://doi.org/10.1016/j.jsamd.2022.100466

nanostructured carriers, which are tailored for enhanced compatibility with the host coating, to self-heal corrosion. The smart autonomous corrosion protection strategy addressing smart delivery of functional species stored in specially designed smart carriers can be easily introduced into protective organic matrices [5–10]. Self-healing coatings for corrosion protection typically include two main healing functionalities [11]: (i) restoration of the polymeric network that allows healing of the barrier properties or (and) (ii) passivation/inhibition of the areas under corrosion, i.e., corrosion prevention/repair. The first functionality is already covered since polyolefin coatings are healable by nature. Concerning the 2nd functionality, it is still lacking in polyolefin coatings; however, this can be achieved using carriers loaded with corrosion inhibitors that allow controlled delivery of the inhibitor and autonomous corrosion repair [11–14].

Many solutions have been proposed in the literature, with some being more advanced than others. The use of microcapsules loaded with corrosion inhibitors has already been state of the art and commercially available. However, most of these capsules are activated by mechanical damage, being fully destroyed during the process of defect formation. The concept is quite interesting for healing polymer matrices, as evidenced by White and co-workers [15,16], but much less attractive for the healing of corroding areas at the steel surface. The reason is simple: scratches that propagate through the polymeric matrix and do not reach the substrate will break a lot of capsules, releasing an inhibitor that is not needed at all. To overcome this disadvantage, there has been intensive research on different smart carriers, such as porous or hollow micro/nanoparticles or hybrid capsules, sensitive to specific stimuli that can control the corrosion inhibitor's release and heal corrosion activity exactly “where and when needed.” Raj, Roma et al. [17] synthesized pH-sensitive hydroxyapatite (HAP) particles loaded with cerium (Ce) ions as a corrosion inhibitor. These modified particles were incorporated into the polyolefin matrix and applied to the pre-treated steel substrate. EIS analysis results demonstrated the long corrosion protection for steel substrate with Ce-HAP. Zhao, Yu et al. [18] successfully synthesized GO/MOFs and encapsulated benzotriazole (BTA) as a corrosion inhibitor. Polyvinyl butyral resin (PVB) was reinforced with GO/MOF-BTA. The corrosion inhibition results demonstrated better corrosion protection due to the excellent barrier properties of GO and the pH-sensitive release of BTA. Bouibed, Aghlis et al. [19] modified the surface of GO with SiO_2 and reinforced it into epoxy to study the barrier properties and corrosion resistance of coatings in 3.5 wt.% NaCl solution. The EIS results demonstrated the enhanced corrosion protection due to the addition of hybrid GO-SiO_2 into epoxy resin. Parok et al. [20] studied the corrosion inhibition performance of BTA on copper surface in 3.5 wt. % NaCl solution. The reported enhanced corrosion inhibition performance of BTA was evident due to the adsorption of BTA on a copper surface. In the above-mentioned literature studies, none of them reported the loading of hybrid particles with functional species. However, in our work, the corrosion inhibition performance of single-layer polyolefin-based coatings reinforced with modified hybrid CeO_2@ZnO particles is reported. The hybrid CeO_2@ZnO particles were successfully synthesized and loaded with benzotriazole (BTA) as a corrosion inhibitor. The successful synthesis and loading of corrosion inhibitors were demonstrated by transmission electron microscopy (TEM), Fourier-transform infrared spectroscopy (FTIR), X-ray diffraction (XRD), and thermogravimetric analysis (TGA) analysis. UV-vis analysis endorsed the pH-sensitive and time-dependent release of corrosion inhibitors from hybrid particles. Corrosion inhibition performance of coatings was demonstrated through Electrochemical impedance spectroscopic analysis (EIS). To the best of our knowledge, this corrosion protection design approach is not reported previously and establishes significant understanding to synthesize more anti-corrosion polyolefin-based coatings.

2. Experimental

2.1. Chemical used

Zinc sulphate heptahydrate ($ZnSO_4 \cdot 7H_2O$), Sodium hydroxide pallets, cerium nitrate Ce $(NO_3)_3 \cdot 6H_2O$, absolute ethanol, Hexamethylene tetramine (HMT), Hydrogen peroxide (H_2O_2), Benzotriazole (BTA as corrosion inhibitor), Sodium Chloride were procured from Sigma Aldrich, and used without further purification. CANVERA™ 1110 Polyolefin used as polymer matrix was purchased from Dow Chemical. Carbon steel coupons ($35 \times 35 \times 0.90$ m^3) employed as substrates (with composition of C = 0.21%, P = 0.30%, S = 0.04%, Cu = 0.20% and Fe = 99.18% and thickness of 1 mm) were obtained from a local supplier. Silicon carbide abrasive paper was purchased from Hebei Yineng pipeline Group Co., Ltd, China.

2.2. Synthesis of CeO_2@ZnO hybrid carriers

2.2.1. Synthesis of ZnO particles from zinc sulphate heptahydrate

9.68 g of $ZnSO_4$. $7H_2O$ was precisely weighed and added to 120 mL of purified water to make starting solution A. 1.6 g of NaOH pellets were added into 40 mL distilled water to make solution B. Solution B was added to solution A in drops with uniform and continue stirring overnight at 800 rpm using a magnetic stirrer. This addition of solution B in the dropwise method is very important for the final structure of ZnO. ZnO precipitates were formed due to the reaction of NaOH with $ZnSO_4$. $7H_2O$ will be filtered using filter paper and then rinsed with distilled water. The precipitates were dried out in a muffle furnace at 100 °C for 6 h. The dried precipitates were ground to a fine powder in a mortar and pestle. The final powder was calcined at 400 °C in the furnace. The appearance of obtained final ZnO particles was white in color.

2.2.2. Synthesis of CeO_2@ ZnO hybrid particles

CeO_2@ZnO hybrid particles were synthesized by the chemical precipitation method, as shown in Fig. 1a. For this, ZnO was used as the core particle. The prepared ZnO particles (2 g) were added into $Ce(NO_3)_3 \cdot 6H_2O$ (4 g) and 60 mL absolute ethanol. This was Solution C. Solution C was placed for ultrasonication for 30 min. Solution D was prepared by dissolving HMT (6.46 g) in 40 mL of purified water. Solution D was added to Solution C, followed by proper agitation at ultrasonicate for 2 h at 75 °C. In this sonication step, 400 μL of H_2O_2 was added to oxidize cerium nitrate into CeO_2 completely. The precipitates were collected, washed with purified water, and dried at 80 °C for 6 h. The dried particles were calcined in the furnace at 500 °C for 2 h. This resulted in the formation of hybrid particles with ZnO as core and CeO_2 as shell particle.

2.2.3. Modification of CeO_2@ZnO hybrid particles with BTA as a corrosion inhibitor

The modification of CeO_2@ZnO hybrid particles with BTA comprised the formulation of a saturated solution of BTA, as represented in Fig. 1b. BTA was dissolved into its solvent (water). CeO_2@ZnO hybrid particles were added to the BTA solution. Thfig1e inhibitor to hybrid particles ratio was kept as 2:1. The solution was placed for continuous stirring with a magnetic stirrer overnight at 700 rpm (25 °C). The solution then underwent vacuum cycling overnight to remove any entrapped air. This step ensures the complete loading of BTA into CeO_2@ZnO hybrid particles. The solution was then centrifuged at 4000 rpm for 15 min to get the resultant modified hybrid particles. The particles were then dried

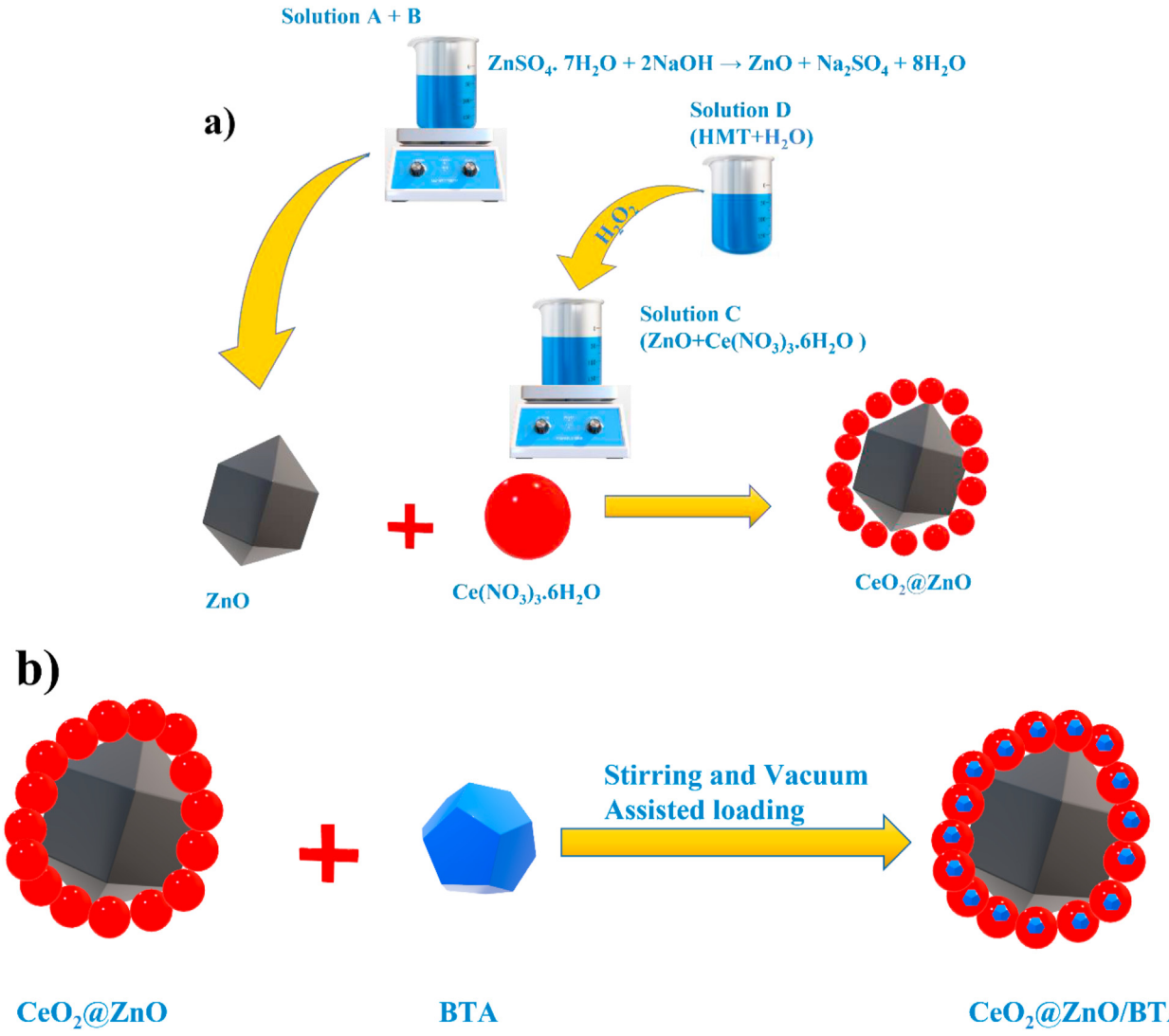

Fig. 1. a) Schematics of synthesis of ZnO and CeO2@ZnO hybrid particles, b) Schematics showing the modification of CeO2@ZnO hybrid particles with BTA by loading process.

up in an oven at 60 °C overnight to ensure complete drying, followed by grounding to obtain fine particles.

2.2.4. Characterization of synthesized hybrid particles and modified hybrid particles

The morphological and elemental analysis of synthesized ZnO, CeO_2@ZnO hybrid particles, and modified CeO_2@ZnO/BTA particles was performed by transmission electron microscopy (TEM, FEI, TALOS F200X, USA) and energy dispersive X-Ray spectroscopy (EDX). The chemical bonding and interaction of synthesized ZnO, CeO_2@ZnO hybrid particles, and modified CeO_2@ZnO/BTA particles were analyzed by employing FTIR Frontier (PerkinElmer, Waltham, MA, USA) spectrometer in the range of 4000−500 cm^{-1}. The weight loss and measurements and thermal stability of synthesized ZnO, CeO_2@ZnO hybrid particles, and modified CeO_2@ZnO/BTA particles were performed utilizing TGA analyzer pyris 4000 (PerkinElmer-USA) ranging from 30 to 1000 °C at the heating rate of 10 °C/min. To study the chemical bonding energy and to get a deep insight into the loading of synthesized hybrid particles, X-ray photoelectron spectroscopy (XPS) (AXIX Ultra DLD, Kratos, UK) was utilized by utilizing a monochromatic X-ray source (Al Kα source). XPS survey spectra were recorded in the binding energy range of 0−800 eV, and the binding energy of C 1s (284.6 eV) was used as a reference. The phases of synthesized ZnO, CeO_2@ZnO hybrid particles, and modified CeO_2@ZnO/BTA particles were examined by employing X-ray diffraction analysis (PANanalytical, Empyrean, Royston, United Kingdom) X′-pert Pro Cu (Ka) with a scanning rate of 2°/min and scanning angle ranging between $10° \leq 2\theta \leq 90°$. UV-Vis spectroscopic analysis (Biochrome Libra S60 double beam spectrophotometer, United Kingdom) was performed to study the pH sensitivity of synthesized hybrid particles and the time-dependent release of the inhibitor from hybrid particles at different pH values. For this aim, 5 mg of product was added into 3.5 wt. % NaCl solution to form a suspension. The pH of the solution was adjusted at 2, 5, 7, 9, and 11 by adding small amounts of HCl or NaOH to adjust the acidic or basic pH.

2.2.5. Preparation of steel substrate

Steel substrates acquired from a local company were polished by engaging a grinding and polishing machine (Metkon ForcoPol IV) and employing SiC abrasive papers (80-2c and 120-2c). The substrates were then dried and cleansed with ethanol to prevent any oxide layer formation and remove dust residue before coating with polyolefin-based coatings.

2.2.6. Synthesis of polyolefin reinforced with modified hybrid particles composite coatings

About one wt. % (with respect to Polyolefin) of hybrid CeO_2@ZnO and modified hybrid CeO_2@ZnO/BTA particles were added to 1 mL of basic water (pH~9) to form a paste-like consistency for better dispersion in the polyolefin matrix. Then this paste was added to water-based Polyolefin while stirring at room temperature @25 °C for 24 h for uniform dispersion of particles and to remove air bubbles. The synthesized Polyolefin reinforced modified hybrid particle mixture was then applied on a polished steel substrate via dip-coating technique. The coatings were then cured at 60 °C for 15 min and then at 170°c for 5 min. The final thickness of coatings was observed as 70 ± 2 μm (Thickness was evaluated by engaging PosiTector 6000) from DeFelsko (Made in the USA). Three different coating formulations were achieved: blank polyolefin coatings labeled as PO coatings (for reference purposes), Polyolefin reinforced with hybrid particles labeled as PO/CeO_2@ZnO, and Polyolefin reinforced with modified hybrid particles labeled as PO/CeO_2@ZnO/BTA for clear evaluation.

2.2.7. Characterization of polyolefin based modified hybrid particles composite coatings

To evaluate the self-healing ability and electrochemical functioning of developed coatings in 0.56 M NaCl solution, the Electrochemical Impedance Spectroscopy (EIS) technique was employed. In this regard, the developed polyolefin-based composite coatings were subjected to EIS testing. The electrochemical measurements were carried out employing Gamry 3000 (30 K BOOSTER Potentiostat/Galvanstate/ZRA, USA), consisting of a three-electrode system. In this study, the coated sample worked as the working electrode, whereas the graphite rod and Ag/AgCl were utilized as the counter and reference electrodes. EIS measurements were commenced after achieving the open circuit potential to a steady value. The frequency range for the EIS experiment was within 0.01Hz−100 kHz, and the RMS signal was 10.0 mV. Gamry E-Chem 3000 software analyzed the measured EIS data, and the suitable equivalent circuits determined fitting parameters. All EIS measurements were executed at 25 °C.

3. Results and discussion

3.1. Morphology and structural analysis

TEM analysis (Fig. 2 (a)) of ZnO revealed the hexagonal morphology of the particles. The particles are mostly in polydisperse form rather than a uniform distribution. However, EDX analysis in Fig. 2 (b) confirmed the presence of Zn and O, which are the main constituents of Zinc oxide, in the final product. In the case of the CeO_2@ZnO, TEM analysis (Fig. 2 (c)) demonstrated that the CeO_2 exhibited spherical morphology with some agglomeration. The particles formed the layer over the ZnO particles and resulted in the formation of a hybrid particle, which is evident from EDX analysis (Fig. 2 (d)). However, the layer formed over ZnO is not very uniform due to agglomeration. EDX confirmed the presence of the main elements of CeO_2 (Ce and O) over ZnO. TEM analysis of particles after being modified from BTA (corrosion inhibitor) (Fig. 2 (e)) demonstrated that the structure of particles became more uniform, exhibiting a more pronounced spherical morphology. EDX analysis (Fig. 2 (f)) confirmed the successful loading of BTA into CeO_2@ZnO.

FTIR analysis represented in Fig. 3a displayed the information regarding the chemical bonding taken place between the different synthesized products. The FTIR spectra of ZnO, CeO_2@ZnO, and CeO_2@ZnO/BTA were recorded in the range of 4000−500 cm^{-1}.

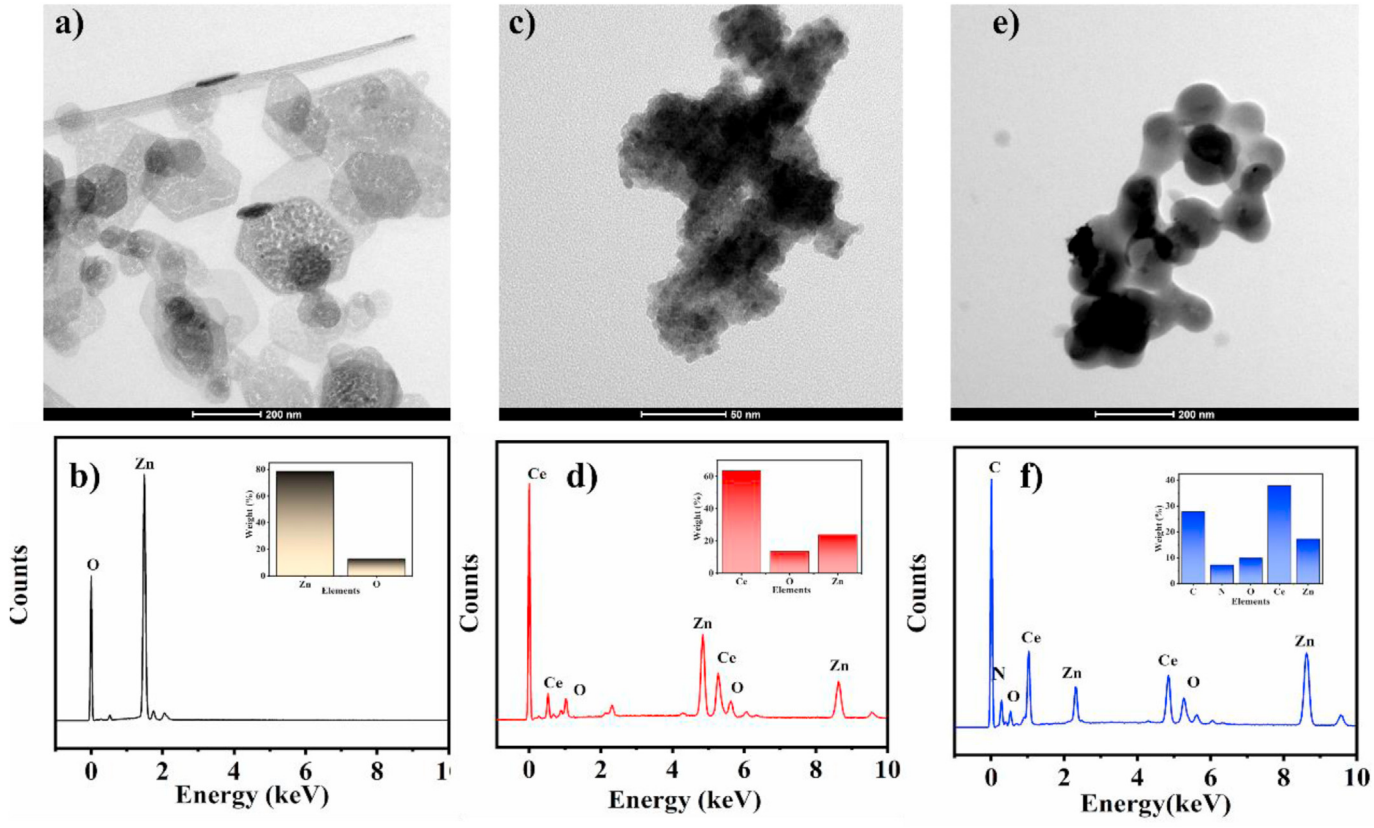

Fig. 2. Transmission electron microscopy (TEM) analysis of (a, c, e) and EDX (b, d, f) analysis of synthesized ZnO, CeO_2@ZnO and CeO_2@ZnO/BTA particles respectively.

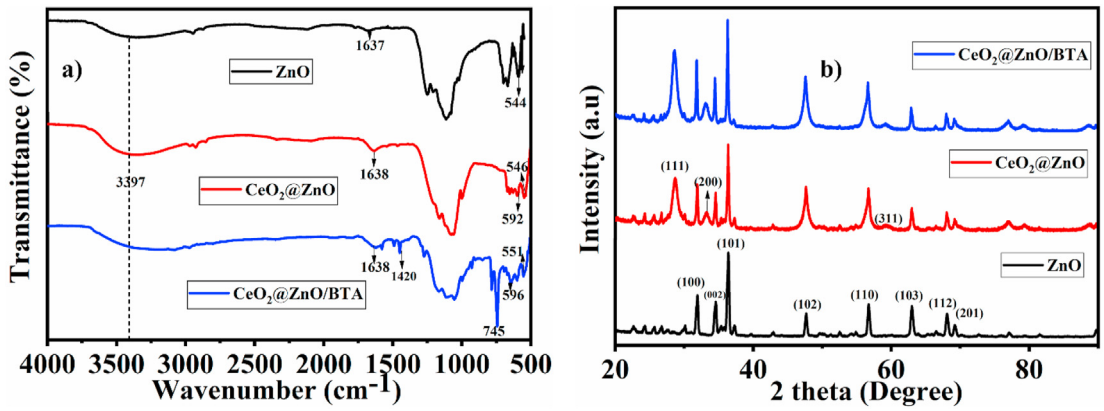

Fig. 3. a) Fourier transform infrared (FTIR) spectra of the synthesized ZnO, CeO_2@ZnO, and CeO_2@ZnO/BTA particles. b) X-ray diffraction (XRD) analysis of the synthesized ZnO, CeO_2@ZnO, and CeO_2@ZnO/BTA particles.

Different functional groups and metal oxide bonding were analyzed from this spectrum to confirm the successful synthesis and loading of the desired product. The broad-spectrum band present at 3397 cm^{-1} is attributed to the O—H group due to physically adsorbed water contents. The small peaks at 1637, 1638, and 1630 cm^{-1} are associated with water molecules (H—O—H) bending vibrations [21]. In the case of ZnO, the peak at 544 cm^{-1} represents the main characteristic peak of metal oxide (Zn—O) bonding which also confirms the successful synthesis of ZnO [22]. The FTIR analysis of the CeO_2@ZnO revealed that the main absorption peaks which confirmed the formation of CeO_2 in hybrid particles were between 500 and 600 cm^{-1}. However, the peak representing the metal oxide stretching vibrations of O—Ce—O can be seen at 592 cm^{-1} [23]. The absorption peak of ZnO represented slight displacement from 544 to 546 cm^{-1} which may be attributed to the reaction between ZnO and CeO_2 particles. The emergence of some more peaks in the case of CeO_2@ZnO/BTA at 1420 and 745 cm^{-1} represented the characteristic aromatic and benzene ring stretching vibrations, respectively [24]. The displacement of ZnO and CeO_2 from 544 to 551 cm^{-1} and from 592 to 596 cm^{-1} reveals the bonding between particles and corrosion inhibitors. The appearance of the main characteristic peaks of BTA and displacement in the distinct peaks of ZnO and CeO_2 is evident from Fig. 4a and a proof of the successful loading of BTA into hybrid particles.

XRD analysis (Fig. 3b) of ZnO particles demonstrated the well-defined peaks positioned at Bragg angle $2\theta^{\circ} = 31.89^{\circ}$, 34.53°,

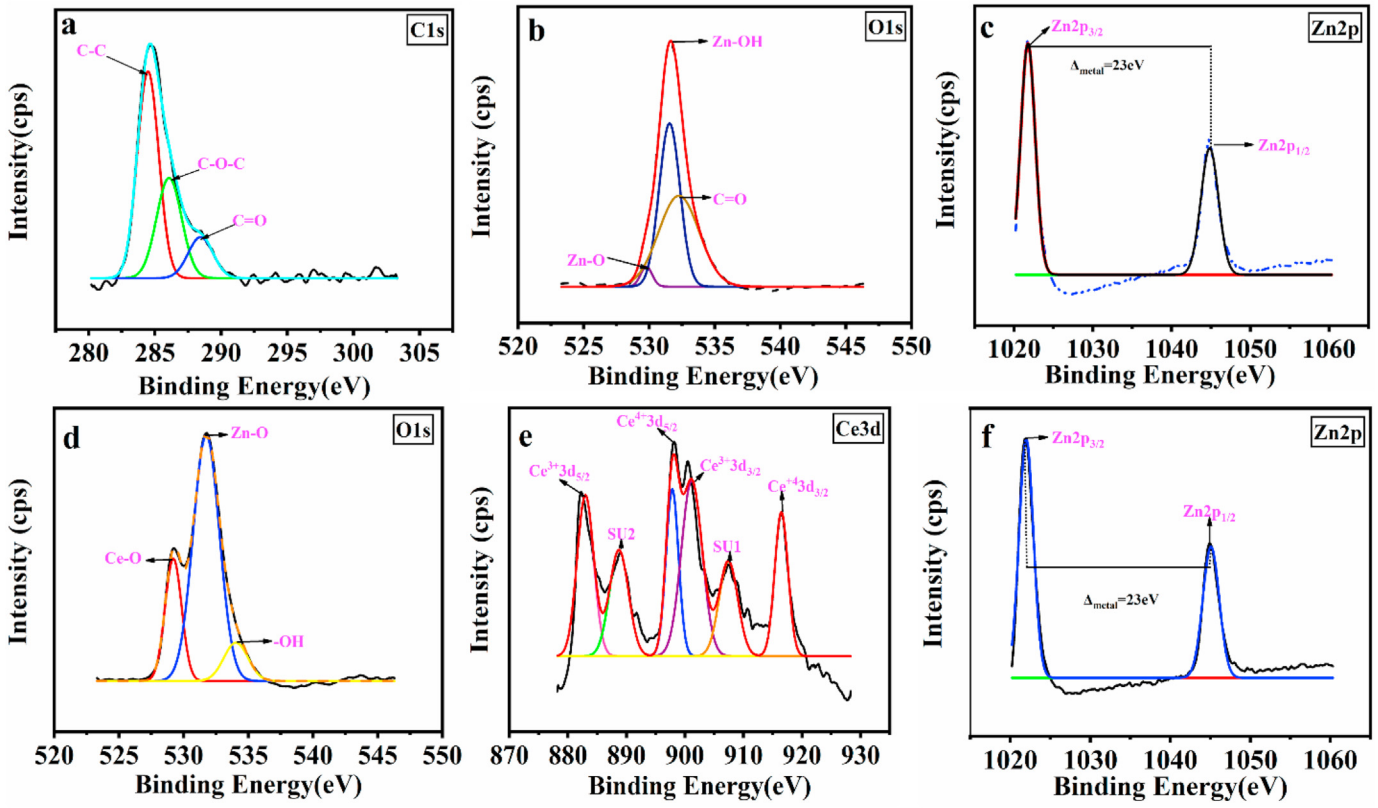

Fig. 4. XPS analysis of ZnO a) C1s, b) O1s, c) Zn2p and CeO_2@ZnO d) O1s, e) Ce3d, and f) Zn2p.

36.37°, 46.77°, 56.72°, 62.95°, 67.99° and 69.15° corresponding to the miller indices plane of hexagonal ZnO that are (100), (002), (102), (110), (103), (112) and (201) respectively (JCPDS 36–1451) [25,26]. After being modified with CeO_2, three distinct diffraction peaks were observed at $2\theta = 28.5°$, 33.1°, and 59.3°, which corresponds to the (111), (200), and (311) planes, respectively. The appearance of the diffraction peaks of the CeO_2 demonstrated the formation of CeO_2 structure in CeO_2@ZnO [27]. In the case of CeO_2@ZnO/BTA, no new diffraction peaks were seen, assuming the interaction of BTA did not affect the crystal structure of synthesized particles.

To analyze the elemental chemical structure and state in synthesized ZnO and CeO_2@ZnO hybrid particles, XPS analysis was employed, as represented in Fig. 4. The carbon element with binding energy 284.6 eV was used as a reference for the calibration and fitting data. The curves were fitted by the nonlinear fitting method linked with the Gaussian distribution function after Tougaard integration background subtraction. The carbon spectra C1s are represented in Fig. 4a. The peak at 284.4eV is assigned to the non-oxygenated C–C bond, while the other two fitted peaks at 286.07 and 288.4eV are associated with oxygenated function groups that are C–O–C and C═O. The O1s spectra in Fig. 4b are convoluted into three peaks. The main peak is observed at a low binding energy of 529.6eV, assigned to Zn–O due to the O^{2-} bonded to Zn^{2+} in the ZnO lattice work. The peak at 531.6 eV is assigned to the loosely bonded oxygen to the surface atoms, such as the hydroxyl group being adsorbed on the surface of ZnO particles. Another peak at 532.26eV is linked with C═O, attributed to the metal carbonates bonding instigated from the adsorbed surface molecules [28]. The Zn spectra in Fig. 4c represent the Zn 2p core-level of Zn peaks. There are two fitted peaks at a binding energy of 1021.7eV and 1044.9 eV, recognized as $Zn2p_{3/2}$ and $Zn2P_{1/2}$, respectively. These two peaks are related to the ZnO particles. The binding energy difference between $Zn2p_{3/2}$ and $Zn2P_{1/2}$ is represented by $\Delta_{metal} = 23$eV, which is also demonstrated as a split spin–orbit component. These studies are also consistent with the previous literature [28,29].

In the case of hybrid CeO_2@ZnO particles, the XPS spectra are displayed in Fig. 4(d and e, f). The Gaussian peak (Fig. 4d) at 529.24eV and 531.77 is attributed to the metal–oxygen bond. The peak at 529.24eV represents the Ce–O bond, and that at 531.77 is related to the Zn–O bond. The peak at 534.07eV is associated with loosely bonded oxygen atoms such as the hydroxy group on the surface. The main peaks of Ce^{4+} shown in Fig. 4e are $Ce^{4+}3d_{5/2}$ and $Ce^{4+}3d_{3/2}$, related to Ce 3 d core spectrum. The two peaks for $Ce^{3+}3d_{5/2}$ and $Ce^{4+}3d_{5/2}$ are represented at 883.07 and 898.21eV, and two peaks for $Ce^{3+}3d_{3/2}$ and $Ce^{4+}3d_{3/2}$ are indicated at 900 and 916.4eV. Two additional lines are specified as 'shake-up' satellite lines, represented as SUI and SU2. The peaks associated with SUI and SU2 are seen at 907.36 and 888.6eV, respectively. These values are in accordance with previously reported studies [30,31]. The presence of Ce as Ce^{3+} indicates oxygen vacancies that are dominant in nanoparticles. These oxygen vacancies are the reason that Ce^{4+} is converted to Ce^{3+}. These values are in accordance with previously reported studies [30,31]. In the case of Zn (Fig. 4f), two Gaussian peaks are seen at 1022 and 1045eV, which are ascribed to the $Zn2p_{3/2}$ and $Zn2p_{1/2}$, respectively. The change in the values of the Zn atom's binding energies indicates that some interaction has been taken place between Zn and other atoms.

3.2. Thermogravimetric analysis of synthesized particles

Thermogravimetric analysis of ZnO, CeO_2@ZnO, CeO_2@ZnO/BTA particles is presented in Fig. 5. The downward trend seen in the TGA analysis curve shows the weight loss/decomposition of the product. The synthesized ZnO shows negligible weight loss till 774 °C. The major degradation peak is seen after 750 °C, showing the decomposition of ZnO to Zinc and oxygen [32]. In the instance of CeO_2@ZnO, the main degradation is also seen after 736 °C.

The high decomposition temperatures of ZnO and CeO_2@ZnO show good thermal stability of synthesized particles. CeO_2@ZnO particles modified with BTA demonstrated weight loss in five different stages. The initial weight loss is noticed in stage ~5%, where T < 200 °C is due to the adsorbed moisture contents in the synthesized particles. In the next stage (200 °C < T < 350 °C), almost 4% weight loss is observed, which is assigned to the initial decomposition of BTA, which continues till the region where T < 450 °C. The main decomposition peak is seen at 437 °C, where almost 26% of weight loss is observed. After that, the weight loss is stable due to thermally stable CeO_2 and ZnO. The weight loss curve also predicts the comparatively high decomposition temperature of BTA (The melting temperature of BTA is 100 °C) because of the shielding of the surface of BTA with hybrid CeO_2@ZnO particles. In brief, it can be determined that when CeO_2@ZnO has been modified from BTA, the total weight loss is observed to be 37%. TGA analysis of CeO_2@ZnO/BTA suggested that BTA has been successfully loaded into CeO_2@ZnO with approximately 24% loading.

3.3. UV-vis spectroscopic analysis of modified CeO_2@ZnO/BTA

3.3.1. Loading and release behavior of inhibitor

To study the loading and release behavior, the inhibitor was loaded into CeO_2@ZnO hybrid particles, as mentioned in section 2.2.3. Fig. 6a represents the UV-vis absorbance spectra of BTA before and after loading into hybrid particles. The BTA before loading and modified hybrid particles (after loading BTA) were suspended in 0.56 M NaCl solution and stirred for 2 h 10 mL of each solution was added into glass cuvettes, and UV spectra were recorded. As observed from Fig. 6a, after loading BTA, the absorbance peak at 261 nm did not change, and no new peaks emerged. But the intensity of the peak was significantly reduced. This decreased intensity indicates the successful loading of BTA into hybrid particles. It is also evidence of a decrease in BTA concentration, which demonstrates BTA loading into hybrid particles. The decrease in absorbance peak intensity also indicates the stability of the BTA molecule after loading [33].

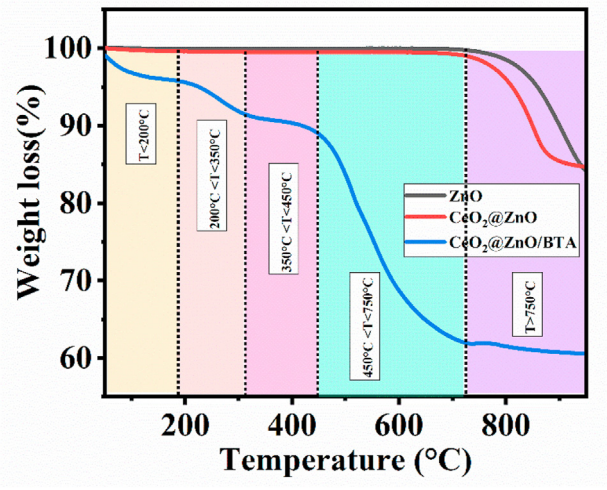

Fig. 5. Thermogravimetric analysis of synthesized ZnO, CeO_2@ZnO, and CeO_2@ZnO/BTA particles.

3.3.2. pH-controlled release of inhibitor at different time intervals

Fig. 6b represents the pH-sensitive and time-dependent release behavior of BTA from CeO_2@Zno hybrid particles in a 0.56 M NaCl medium. The modified CeO_2@ZnO/BTA particles were dissolved in 0.56 M NaCl solution at different pH values (2, 5, 7, 9, 11) by adjusting the pH of the solution. The UV-vis spectra were recorded at different time periods (24, 48, 72, 96 h), as represented in Fig. 6b. The main absorption peak of BTA can be seen at 209 and 261 nm (inset of Fig. 6b). The absorbance peak at this wavelength relates to the n-π* and π-π* transition of the aromatic ring in BTA [34]. It is evident from the UV spectra that BTA demonstrated better release in the acidic and neutral medium as compared to the basic medium. So BTA was proved to be a better inhibitor in the acidic or neutral medium [35,36].

Moreover, CeO_2 also decomposes at acidic pH triggering the release of BTA [37]. After the decomposition of CeO_2, the pronounced release of inhibitor in an acidic medium is related to the fact that the BTA possesses a nitrogen atom with three lone pairs of electrons. The nitrogen atoms in BTA can be easily protonated. Thus, there will be electrostatic interaction between Chloride (Cl^-) ions of NaCl solution. Moreover, looking at the spectra, we can conclude that the inhibitor release is time-dependent. Over time the intensity of the inhibitor being released is also increasing.

3.4. Electrochemical impedance spectroscopic analysis of coatings

The corrosion mitigation performance for blank Polyolefin, PO/CeO_2@ZnO, and PO/CeO_2@ZnO/BTA coatings were studied by electrochemical impedance spectroscopic analysis technique in 0.56 M NaCl solution over the period of 24, 48, 72, 96 and 120 h. EIS is the non-destructive technique to evaluate the corrosion inhibition functioning of polymeric coatings. The data (bode and phase angle plot) assimilated through EIS after different immersion times are shown in Fig. 8 and assimilated in the table represented in Table S1. An impedance test for each coating was done three times to ensure reproducible results. The equivalent circuit established for fitting data is illustrated in Fig. 7 with two times constant for blank polyolefin coatings and two times constant and Warburg diffusion constant for modified coatings. The various parameters obtained from the equivalent circuit are given as R_{po} (pore resistance), R_{ct} (charge transfer resistance), CPE1 (capacitance with pore resistance), CPE2 (capacitance associated with charge transfer resistance), and W (Warburg diffusion constant) corresponds to the mass transfer. The constant phase elements of the coatings and double layer at the metal/coating boundary are correspondingly represented as CPE1 and CPE2.

The bode and phase angle plots for blank polyolefin coatings at various time intervals of (24, 48, 72, 96, and 120 h) are represented in Fig. 8a. The low-frequency impedance at $|Z_{0.01Hz}|$ demonstrates

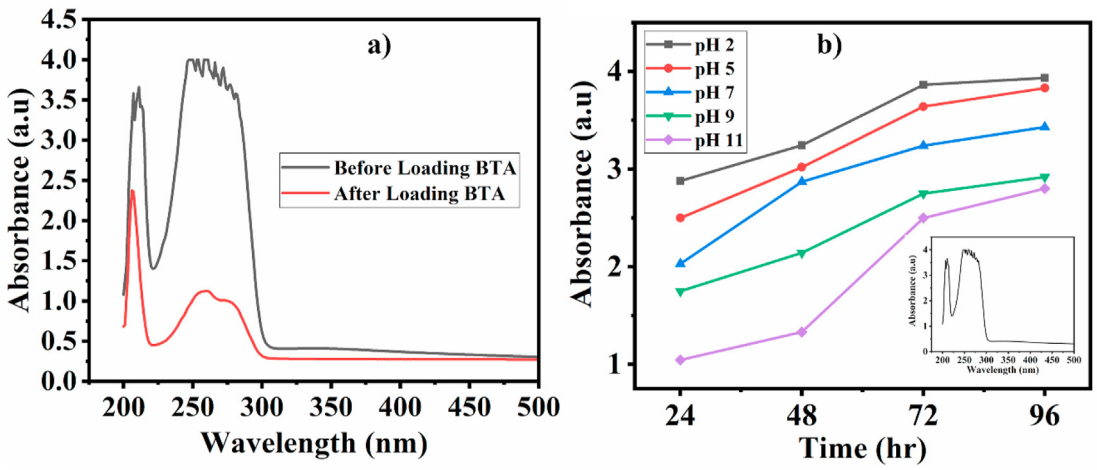

Fig. 6. (a) UV-vis spectra of BTA before and after loading in CeO_2@ZnO in 3.5 wt. % NaCl solution; (b) pH responsive behavior of BTA at different pH (2, 5, 7, 9 11) and different time intervals (24, 48, 72, 96 h) in 3.5 wt. % NaCl solution.

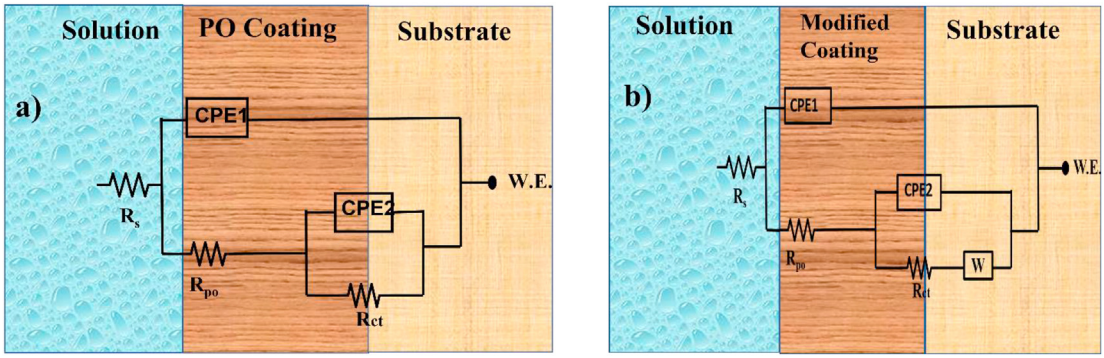

Fig. 7. Equivalent circuit used to fit data for a) blank polyolefin coatings and b) modified coatings.

the protective capacity of coatings. In the case of blank polyolefin coatings, the impedance value at 24 h of immersion is 9.10 GOhm.cm2 and highest compared to the rest of the days. With the gradual increase in the immersion time, the impedance value or protective behavior of blank polyolefin coatings started to decrease to 0.04 GOhm.cm^{2,} explicating the deterioration of coatings. Two capacitance loops can be noticed (phase angle plot (Fig. 8b)), which decrease with the immersion time, displaying the diminution in capacitance behavior. Due to the decrease in the impedance values, the capacitance of the coating is increasing. The relation between these two is opposite. The increase in the values of CPE1 and CPE2 (as represented in Table S1) demonstrates the depreciation of coatings. The decrease in the protective behavior of blank polyolefin coatings indicates that electrolytes form conductive paths due to the porosity or existence of pores in coatings. These conductive paths facilitate corrosion propagation; over time, the corrosion rate increases due to the continuous contact of electrolytes with steel.

In the case of the PO/CeO_2@ZnO coatings, the protective performance of coatings is enhanced compared to the blank polyolefin

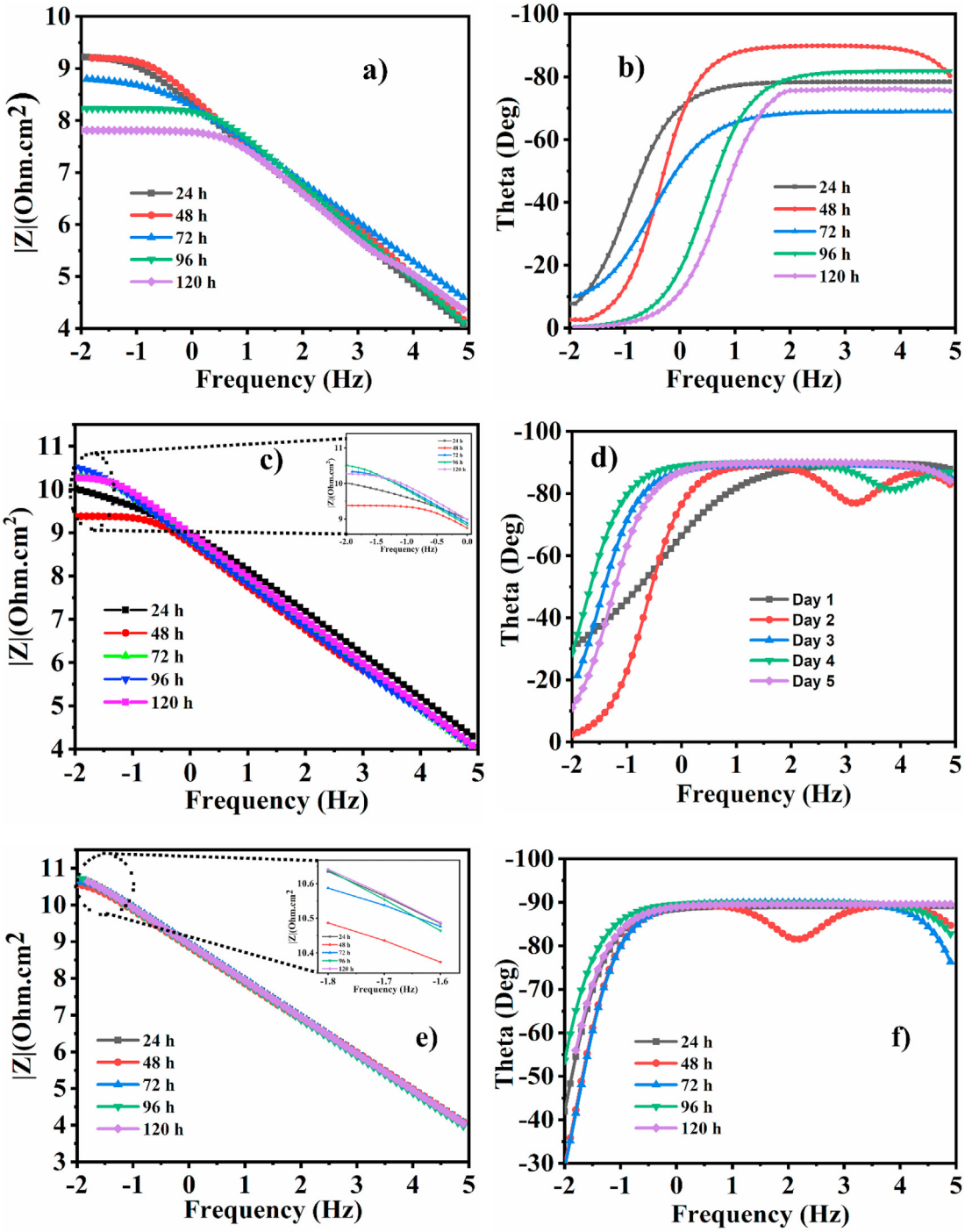

Fig. 8. EIS bode and phase angle plots of (a, b) Blank polyolefin, (c, d) PO/CeO_2@ZnO, and (e, f) 0.56 M NaCl solution for the period of 24, 48, 72, 96, and 120 h.

coatings. The bode and phase angle plots for these coatings are represented in Fig. 8c, d. The bode plots for PO/CeO_2@ZnO coatings indicate an increase in the impedance values with immersion time. During 24 h of immersion time, the impedance value at low frequency is observed to be 33.4 GOhm.cm^2. After 24 h, the value decreased to 2.40 GOhm.cm^2 due to the formation of corrosion species. With the increase in the immersion time, the impedance value is also increased such that after 96 h of immersion time, the impedance value is observed to be 28.8 GOhm.cm^2. After 120 h of immersion, the impedance value again decreases, but the value is still in GOhm, so that it can be neglected. The phase angle plot after 120 h of immersion is noticed to be near 85°, demonstrating the capacitive behavior. The protective ability of PO/CeO_2@ZnO coatings is ascribed to CeO_2@ZnO hybrid particles in polyolefin matrix, which increased the barrier properties of the matrix by pervading the pores. The increase in the impedance values at the low-frequency range with time decreased the CPE1 and CPE2 values. The decrease in the constant phase elements values also reveals the protective behavior of PO/CeO_2@ZnO coatings.

In the case of PO/CeO_2@ZnO/BTA coatings, the bode and phase angle plots are shown in Fig. 8e, f. The impedance values at $|Z_{0.01\ Hz}|$ that is a low-frequency range, after 24 h of immersion, are observed to be 58.3 GOhm.cm^2. The impedance values are close to the 10^{11} Ohm. cm^2 since 24 h of immersion. The value decreased slightly after 24 h but remained above 10^9 Ohm. cm^2. The phase angle plots revealed the capacitive response of coatings, as the phase angle is observed at 90°. The equivalent circuit represented the two-time constant coating behavior and corrosion activity at the metal/coating interface at the low and high-frequency range. Both PO/CeO_2@ZnO and PO/CeO_2@ZnO/BTA demonstrated good barrier and protective properties. However, the PO/CeO_2@ZnO/BTA exhibited exceptional protective behavior compared to the blank Polyolefin and PO/CeO_2@ZnO coatings. The remarkable barrier properties of PO/CeO_2@ZnO/BTA coatings are due to the formation of the passive protective layer of inhibitor at the defect site. The decrease in the CPE values with an increase in immersion time is an indication that BTA got adsorbed on the metal surface. The nitrogen element in the BTA structure possesses a lone pair of electrons that have an affinity to form a bond with the vacant d-orbital of Fe of steel. Also, from the results obtained from UV analysis Fig. 6b, the BTA showed a more pronounced release in acidic pH. As pH decreases, more inhibitor is released over time. The mechanism of corrosion inhibitor on steel/coating interface involves the formation of Fe^{2+} ions due to the anodic dissolution followed by the localized change in pH and release of inhibitor due to a decrease in pH at the defect site. The self-healing mechanism is described in section 3.4.1.

The variation in R_{po} and R_{ct} values for blank Polyolefin, PO/CeO_2@ZnO, and PO/CeO_2@ZnO/BTA coatings is represented in Fig. 9 (a, c). The pore resistance values for the blank polyolefin coatings decrease with the increase in the immersion time, validating the deterioration of coatings due to more water uptake, which also resulted in the removal of coating at the metal/coating interface. For the PO/CeO_2@ZnO and PO/CeO_2@ZnO/BTA, the R_{po} and R_{ct} values increase with the immersion time, which is considered due to the improved corrosion performance of barrier properties. The values of R_{po} and R_{ct} of PO/CeO_2@ZnO/BTA are comparatively higher than PO/CeO_2@ZnO coatings due to the presence of corrosion inhibitors (BTA). Moreover, the incorporation of modified

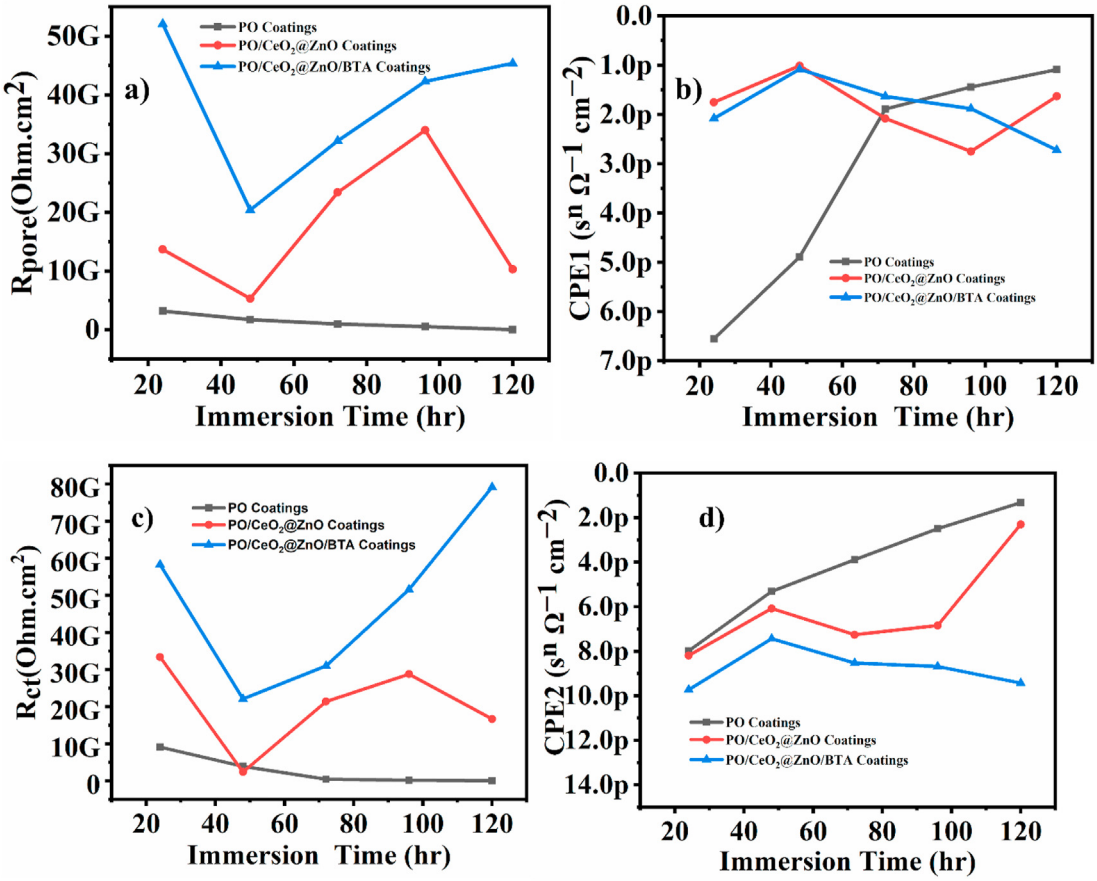

Fig. 9. Evolution of fitting parameters obtained from EIS data a) Pore resistance, b) Capacitance CPE1, c) Charge transfer resistance R_{ct} and d) Capacitance CPE2 during the period of 24, 48, 72, 96, and 120 h.

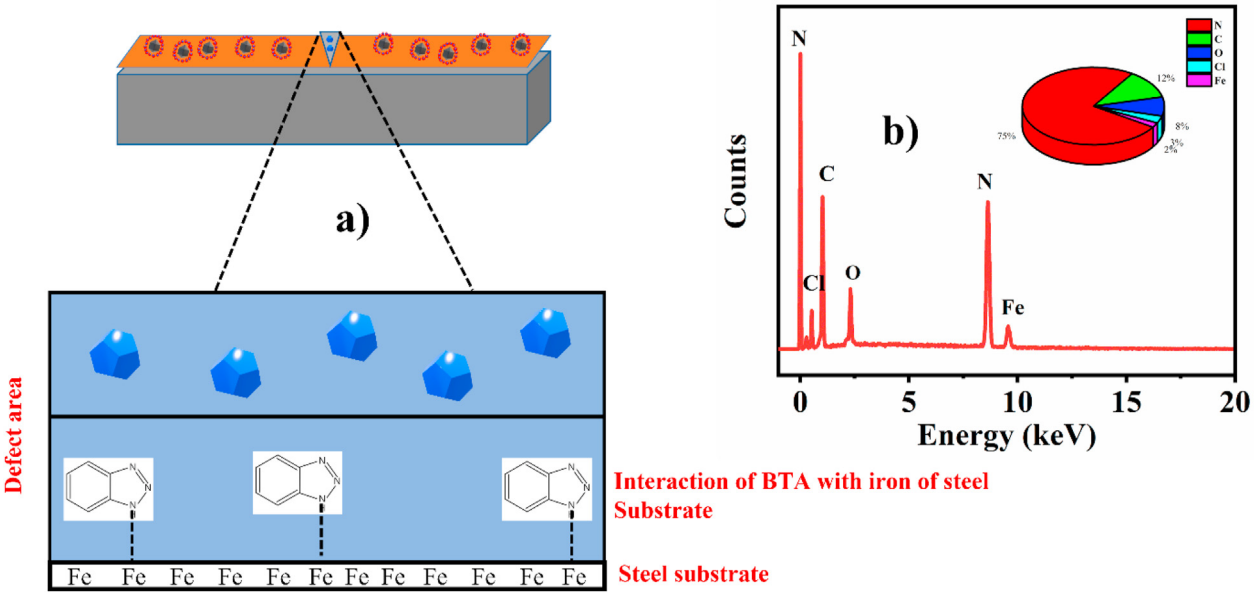

Fig. 10. a) Schematics demonstrating the Self-healing mechanism of Polyolefin based composite coatings modified with modified hybrid CeO_2@ZnO particles, b) EDX analysis of the steel after delamination of steel at metal/coating interface.

hybrid particles also preserved the polyolefin matrix. The evolution data obtained from CPE1 and CPE2 for modified coatings are represented in Fig. 9(c and d). The increase in impedance values and decrease in CPE values with immersion time are evident from the protective behavior of coatings. After 24 h, the increase in CPE values is seen due to the water uptake, but this increase is significantly very low, which was later balanced by an increase in the R_{po} and R_{ct} values with an increase in immersion time, demonstrating the corrosion inhibition effect.

3.4.1. Self-healing mechanism of polyolefin based composite coating

The inhibitive performance of the organic compounds, which mainly possess Sulphur, nitrogen, and oxygen, is because of the formation of a coordinate bond. The bond is shared between the metal and the lone pair of electrons of the inhibitive species. BTA adsorption on the metal surface develops due to the interaction of π-electrons of inhibitor and vacant d-orbitals of metal (Fe) surface. The presence of nitrogen and π-electrons on the aromatic ring in the BTA is responsible for corrosion inhibition performance. These considerations are essential for the adsorption of inhibitors on the metal surface [35]. Due to the change in pH, the inhibitor is released from carriers and moves towards the defect site. Over there, the presence of Fe^{2+} interacts with the nitrogen with lone pair of electrons of the inhibitor, which results in the formation of the passive layer at the defect site. The corrosion propagation is initiated due to the interaction of chloride ions followed by the appearance of $Fe^{2+,}$ which then interacts with the inhibitor species [38,39]. The schematics showing the self-healing mechanism of Polyolefin-based composite coatings reinforced with modified hybrid are represented in Fig. 10a. The EDX analysis was employed to confirm the presence of inhibitor at the metal/coating interface Fig. 10b. For this purpose, the cross-sectional area of coatings was examined by making a scratch in the coating, and analysis was performed on steel. The presence of main elements of inhibitor (Nitrogen and Carbon) are identified, confirming the release of inhibitor. There are traces of chloride due to the electrolyte (NaCl) and Fe of the steel. The inset shows the weight percentage of the identified elements.

4. Conclusion

The hybrid particles CeO_2@ZnO were successfully synthesized, followed by the modification with benzotriazole (corrosion inhibitor). The modified hybrid particles were incorporated into the polyolefin matrix at a concentration of 1 wt. %. A single-layer coating system was synthesized. Different characterization techniques (EDX, TEM, FTIR, TGA, and XPS) were employed to confirm the successful synthesis of the hybrid particles and the loading of inhibitors into the hybrid particles. UV-vis spectroscopic analysis supports the evidence of the time-dependent and pH-sensitive release of the inhibitor from the hybrid particles. EIS analysis demonstrates the excellent barrier properties of modified coatings compared to the blank polyolefin coatings. The exceptional corrosion inhibition performance of the modified coatings is related to the efficient release of inhibitors at different immersion times in response to the change in the external trigger.

Funding

This research was funded by the Qatar National Research Fund (a member of the Qatar Foundation), grant number NPRP Grant 11S−1226-170132. Statements made herein are solely the responsibility of the authors.

Data availability

The raw/processed data required to reproduce these findings cannot be shared at this time due to legal or ethical reasons.

Declaration of competing interest

The authors declare that they have no known competing financial interests or personal relationships that could have appeared to influence the work reported in this paper.

Acknowledgment

The authors would like to thank the Central laboratory Unit (CLU), Qatar University, 2713, Doha, Qatar, for the TEM analysis facility and the Gas processing center (GPC), Qatar University, 2713, Doha, for the XPS analysis faculty.

Appendix A. Supplementary data

Supplementary data to this article can be found online at https://doi.org/10.1016/j.jsamd.2022.100466.

References

[1] D. Webster, Pipeline construction drivers , corrosion costs and engineering issues, NAPCA Conv (2010) 1–77.
[2] C.I. Ossai, B. Boswell, I.J. Davies, Pipeline failures in corrosive environments - a conceptual analysis of trends and effects, Eng. Fail. Anal. 53 (2015) 36–58, https://doi.org/10.1016/j.engfailanal.2015.03.004.
[3] F.M. Galogahi, Y. Zhu, H. An, N.-T. Nguyen, Core-shell microparticles: generation approaches and applications, J. Sci. Adv. Mater. Devices. 5 (2020) 417–435, https://doi.org/10.1016/j.jsamd.2020.09.001.
[4] H. Vugteveen, Amorphous Polyolefin Coatings, vol. 2017, Eurocorr, 2017, p. 1.
[5] D. Snihirova, S.V. Lamaka, M.M. Cardoso, J.A.D. Condeço, H.E.C.S. Ferreira, M. De Fatima Montemor, PH-sensitive polymeric particles with increased inhibitor-loading capacity as smart additives for corrosion protective coatings for AA2024, Electrochim. Acta 145 (2014) 123–131, https://doi.org/10.1016/j.electacta.2014.09.009.
[6] D. Snihirova, S.V. Lamaka, P. Taheri, J.M.C. Mol, M.F. Montemor, Comparison of the synergistic effects of inhibitor mixtures tailored for enhanced corrosion protection of bare and coated AA2024-T3, Surf. Coating. Technol. 303 (2016) 342–351, https://doi.org/10.1016/j.surfcoat.2015.10.075.
[7] S. Habib, E. Fayyed, R.A. Shakoor, R. Kahraman, A. Abdullah, Improved self-healing performance of polymeric nanocomposites reinforced with talc nanoparticles (TNPs) and urea-formaldehyde microcapsules (UFMCs), Arab. J. Chem. 14 (2021) 102926, https://doi.org/10.1016/j.arabjc.2020.102926.
[8] S. Habib, A. Hassanein, R. Kahraman, E. Mahdi Ahmed, R.A. Shakoor, Self-healing behavior of epoxy-based double-layer nanocomposite coatings modified with Zirconia nanoparticles, Mater. Des. 207 (2021) 109839, https://doi.org/10.1016/j.matdes.2021.109839.
[9] M. Nawaz, R.A. Shakoor, R. Kahraman, M.F. Montemor, Cerium oxide loaded with gum Arabic as environmentally friendly anti-corrosion additive for protection of coated steel, Mater. Des. 198 (2020) 109361, https://doi.org/10.1016/j.matdes.2020.109361.
[10] A. Khan, A. Hassanein, S. Habib, M. Nawaz, R.A. Shakoor, R. Kahraman, Hybrid halloysite nanotubes as smart carriers for corrosion protection, ACS Appl. Mater. Interfaces 12 (2020) 37571–37584, https://doi.org/10.1021/acsami.0c08953.
[11] M.F. Montemor, Functional and smart coatings for corrosion protection: a review of recent advances, Surf. Coating. Technol. 258 (2014) 17–37, https://doi.org/10.1016/J.SURFCOAT.2014.06.031.
[12] T. Matsuda, N. Jadhav, K.B. Kashi, M. Jensen, A. Suryawanshi, V.J. Gelling, Self-healing ability and particle size effect of encapsulated cerium nitrate into pH sensitive microcapsules, Prog. Org. Coating 90 (2016) 425–430, https://doi.org/10.1016/j.porgcoat.2015.10.021.
[13] T. Szabó, J. Telegdi, L. Nyikos, Linseed oil-filled microcapsules containing drier and corrosion inhibitor - their effects on self-healing capability of paints, Prog. Org. Coating 84 (2015) 136–142, https://doi.org/10.1016/j.porgcoat.2015.02.020.
[14] F. Cotting, I.V. Aoki, Smart protection provided by epoxy clear coating doped with polystyrene microcapsules containing silanol and Ce (III) ions as corrosion inhibitors, Surf. Coating. Technol. 303 (2016) 310–318, https://doi.org/10.1016/j.surfcoat.2015.11.035.
[15] S.R. White, N.R. Sottos, P.H. Geubelle, J.S. Moore, M.R. Kessler, S.R. Sriram, E.N. Brown, S. Viswanathan, Autonomic healing of polymer composites, Nature 409 (2001) 794–797, https://doi.org/10.1038/35057232.
[16] E.N. Brown, N.R. Sottos, S.R. White, Fracture testing of a self-healing polymer composite, Exp. Mech. 42 (2002) 372–379, https://doi.org/10.1007/bf02412141.
[17] R. Raj, M.G. Taryba, Y. Morozov, R. Kahraman, R.A. Shakoor, M.F. Montemor, On the synergistic corrosion inhibition and polymer healing effects of polyolefin coatings modified with Ce-loaded hydroxyapatite particles applied on steel, Electrochim. Acta 388 (2021) 138648, https://doi.org/10.1016/j.electacta.2021.138648.
[18] Y. Zhao, F. Jiang, Y.Q. Chen, J.M. Hu, Coatings embedded with GO/MOFs nanocontainers having both active and passive protecting properties, Corrosion Sci. 168 (2020) 108563, https://doi.org/10.1016/j.corsci.2020.108563.
[19] A. Bouibed, R. Doufnoune, Synthesis and characterization of hybrid materials based on graphene oxide and silica nanoparticles and their effect on the corrosion protection properties of epoxy resin coatings, J. Adhes. Sci. Technol. 33 (2019) 834–860, https://doi.org/10.1080/01694243.2019.1571660.
[20] P.F. Khan, V. Shanthi, R.K. Babu, S. Muralidharan, R.C. Barik, Effect of benzotriazole on corrosion inhibition of copper under flow conditions, J. Environ. Chem. Eng. 3 (2015) 10–19, https://doi.org/10.1016/j.jece.2014.11.005.
[21] N.C. Wu, E.W. Shi, Y.Q. Zheng, W.J. Li, Effect of pH of medium on hydrothermal synthesis of nanocrystalline cerium(IV) oxide powders, J. Am. Ceram. Soc. 85 (2002) 2462–2468, https://doi.org/10.1111/j.1151-2916.2002.tb00481.x.
[22] S. Mallakpour, M. Madani, Use of silane coupling agent for surface modification of zinc oxide as inorganic filler and preparation of poly(amide-imide)/zinc oxide nanocomposite containing phenylalanine moieties, Bull. Mater. Sci. 35 (2012) 333–339, https://doi.org/10.1007/s12034-012-0304-8.
[23] S. Habib, E. Fayyad, M. Nawaz, A. Khan, R.A. Shakoor, Cerium Dioxide Nanoparticles as Smart Carriers for Self-Healing Coatings Cerium Dioxide Nanoparticles as Smart Carriers for Self-Healing Coatings, 2020, https://doi.org/10.3390/nano10040791.
[24] M.M. Mennucci, E.P. Banczek, P.R.P. Rodrigues, I. Costa, Evaluation of benzotriazole as corrosion inhibitor for carbon steel in simulated pore solution, Cement Concr. Compos. 31 (2009) 418–424, https://doi.org/10.1016/j.cemconcomp.2009.04.005.
[25] K. Handore, S. Bhavsar, A. Horne, P. Chhattise, K. Mohite, J. Ambekar, N. Pande, V. Chabukswar, Novel green route of synthesis of ZnO nanoparticles by using natural biodegradable polymer and its application as a catalyst for oxidation of aldehydes, J. Macromol. Sci. Part A Pure Appl. Chem. 51 (2014) 941–947, https://doi.org/10.1080/10601325.2014.967078.
[26] V.R. Venu Gopal, S. Kamila, Effect of temperature on the morphology of ZnO nanoparticles: a comparative study, Appl. Nanosci. 7 (2017) 75–82, https://doi.org/10.1007/s13204-017-0553-3.
[27] S. Xunwen, Z. Liqun, L. Weiping, L. Huicong, Y. Hui, The synthesis of monodispersed M-CeO2/SiO2 nanoparticles and formation of UV absorption coatings with them, RSC Adv. 10 (2020) 4554–4560, https://doi.org/10.1039/c9ra08975f.
[28] C. Wang, H. Fan, X. Ren, J. Fang, Room temperature synthesis and enhanced photocatalytic property of CeO2/ZnO heterostructures, Appl. Phys. Mater. Sci. Process 124 (2018) 1–12, https://doi.org/10.1007/s00339-017-1543-8.
[29] R. Al-Gaashani, S. Radiman, A.R. Daud, N. Tabet, Y. Al-Douri, XPS and optical studies of different morphologies of ZnO nanostructures prepared by microwave methods, Ceram. Int. 39 (2013) 2283–2292, https://doi.org/10.1016/j.ceramint.2012.08.075.
[30] H. Li, G. Wang, F. Zhang, Y. Cai, Y. Wang, I. Djerdj, Surfactant-assisted synthesis of CeO2 nanoparticles and their application in wastewater treatment, RSC Adv. 2 (2012) 12413–12423, https://doi.org/10.1039/C2RA21590J.
[31] B. Pandit, B.R. Sankapal, P.M. Koinkar, Novel chemical route for CeO 2/MWCNTs composite towards highly bendable solid-state supercapacitor device, Sci. Rep. 9 (2019) 1–13, https://doi.org/10.1038/s41598-019-42301-y.
[32] T. Imoto, Y. Harano, Y. Nishi, The thermal decomposition of zinc oxide, Bull. Chem. Soc. Jpn. 37 (1964) 1181–1186, https://doi.org/10.1246/bcsj.37.1181.
[33] C. Arunchandran, S. Ramya, R.P. George, U. Kamachi Mudali, Self-healing corrosion resistive coatings based on inhibitor loaded TiO 2 nanocontainers, J. Electrochem. Soc. 159 (2012) C552–C559, https://doi.org/10.1149/2.020212jes.
[34] A.C. Borin, L. Serrano-Andrés, V. Ludwig, S. Canuto, Theoretical absorption and emission spectra of 1H- and 2H-benzotriazole, Phys. Chem. Chem. Phys. 5 (2003) 5001–5009, https://doi.org/10.1039/b310702g.
[35] S.T. Selvi, V. Raman, N. Rajendran, Corrosion inhibition of mild steel by benzotriazole derivatives in acidic medium, J. Appl. Electrochem. (2003) 1175–1182.
[36] A. Popova, M. Christov, Evaluation of impedance measurements on mild steel corrosion in acid media in the presence of heterocyclic compounds, Corrosion Sci. 48 (2006) 3208–3221, https://doi.org/10.1016/j.corsci.2005.11.001.
[37] M.F. Montemor, C. Vicente, I.S. Técnico, Functional Self-Healing Coatings : A New Trend in Corrosion Protection by Organic Coatings, Elsevier, 2018, https://doi.org/10.1016/B978-0-12-409547-2.13442-0.
[38] S. Habib, E. Fayyed, A. Shakoor, A. Kahraman, Ramazan Abdullah, Improved self-healing performance of polymeric nanocomposites reinforced with talc nanoparticles (TNPs) and urea-formaldehyde microcapsules (UFMCs), Arab. J. Chem. 14 (2020) 102926, https://doi.org/10.1016/j.arabjc.2020.102926.
[39] K. Sabet Bokati, C. Dehghanian, Adsorption behavior of 1H-benzotriazole corrosion inhibitor on aluminum alloy 1050, mild steel and copper in artificial seawater, J. Environ. Chem. Eng. 6 (2018) 1613–1624, https://doi.org/10.1016/j.jece.2018.02.015.